G. Gori, O.P. Le Maitre, P.M. Congedo
On the Sensitivity of Structural Turbulence Uncertainty Estimates to Time and Space Resolution
Computers & Fluids, Vol. 229, 2021, 105081 (9 pages)
doi:10.1016/j.compfluid.2021.105081

On the Sensitivity of Structural Turbulence Uncertainty Estimates to Time and Space Resolution

G. Gori[a,c,*], O.P. Le Maître[a,b,c], P.M. Congedo[a,c]

[a] *INRIA*
[b] *CNRS*
[c] *Centre de Mathématiques Appliquées, École Polytechnique, IPP, Route de Saclay, 91128 Palaiseau, France*

Abstract

This paper presents a sensitivity analysis of structural turbulence uncertainty estimates to time and space resolution of numerical computations. Turbulence uncertainty estimates are obtained by means of the Eigenspace Perturbation Method (EPM). Results show that, in general, one can not expect the turbulence uncertainty estimates to be mesh and time-step independent based on the sole sensitivity analysis of the baseline solution. The recommendation is to carry out independent sensitivity studies, to guarantee that the confidence uncertainty estimates are well-predicted regardless of the space and time resolution.

Keywords: Uncertainty Quantification, Eigenspace Perturbation Method, Turbulence closure uncertainty

1. Introduction

The popular Reynolds-Averaged Navier-Stokes (RANS) model for Computational Fluid Dynamics (CFD) consists of partial differential equations

*Corresponding author: giulio.gori@inria.fr

derived from the time-averaging of the Navier-Stokes model for fluid flows. Unfortunately, turbulence closures are required to model the Reynolds Stress Tensor (RST), which accounts for the time-average of the non-linear convective term. Typically, closures rely on strong inherent model-form assumptions that limit the fidelity of CFD predictions, especially for flows characterized by a pronounced streamline curvature or adverse pressure gradients (Duraisamy et al., 2019). Also, the direct quantification of the errors introduced in turbulent modeling is demanding, if not just intractable. Nowadays, formal and practical Uncertainty Quantification (UQ) techniques in turbulence applications are becoming available (see Xiao and Cinnella (2019) for a comprehensive review). Among these techniques, Eigenspace Perturbation Methods (EPM) (Emory et al., 2011, 2013; Iaccarino et al., 2017) are designed to obtain reasonable and informed uncertainty estimates of selected Quantity of Interest (QOIs) of the turbulent flow. Note the deliberate use of the word *estimation*, rather than *quantification*, implying the computation of uncertainty estimates rather than rigorous and provable bounds on the prediction. However, it is essential to compute these estimates with sufficient accuracy to draw meaningful conclusions from the uncertainty analysis.

This paper investigates the sensitivity of the EPM uncertainty estimates to the time and space resolution of computational simulations. The reference test case is the classical two-dimensional NACA 0012 airfoil. The paper is structured as follows: Sec. 2 summarizes the critical points of the EPM formulation. Section 3 describes the computational model, the physical characteristics of the problem, and the numerical setting of CFD simulations. Section 4 presents the results. Eventually, Sec. 5 summarizes the findings

and provides recommendations for future applications.

2. Eigenspace Perturbation Method

The Reynolds Stress Tensor (RST) results from the decomposition of the time-averaged non-linear convective term of the Navier-Stokes model for fluids. The RST entries are the correlations between the fluctuating velocity components u_i of the flow,

$$\langle u_i u_j \rangle \approx \langle u_i u_j \rangle^{BS}, \tag{1}$$

where the angular brackets indicate the time-average of the argument. The components of the RST are usually approximated using semi-empirical closures. From now on, we will refer to such closures as the baseline ones (BS). By definition, the RST is symmetric positive semi-definite and, therefore, it must fulfill the following set of realizability conditions (Simonsen and Krogstad, 2005; Schumann, 1977)

$$\langle u_i u_i \rangle \geq 0, \quad \langle u_i u_i \rangle + \langle u_j u_j \rangle \geq |2 \langle u_i u_j \rangle|, \quad \det\left(\langle \mathrm{u_i u_j} \rangle\right) \geq 0. \tag{2}$$

Notoriously, the RST is decomposed into an anisotropy and a deviatoric part

$$\langle u_i u_j \rangle = 2k \left(b_{ij} + \frac{\delta_{ij}}{3} \right). \tag{3}$$

Naturally, the realizability conditions (2) must apply also to the anisotropy tensor b_{ij}. The anisotropy tensor can be expressed in spectral form

$$b_{ij} = v_{ik} \Lambda_{kl} v_{jl}, \tag{4}$$

being v_{ik} and v_{jl} the left and the right eigenvectors whereas Λ_{kl} is a diagonal matrix containing the eigenvalues λ_i in a decreasing order. The EPM

consists in applying perturbations of finite amplitude to the RST eigenspace, during the CFD solution iterations, yet fulfilling the realizability conditions. Namely, possible perturbations consist in increasing/decreasing the amount of turbulent kinetic energy, in varying the anisotropy tensor spectral distribution, or in changing the orientation of the anisotropy tensor basis. Hereinafter, we will take advantage of superscript * to point out a perturbed entity

$$\langle u_i u_j \rangle^* = 2k^* \left(v^*_{ik} \Lambda^*_{kl} v^*_{jl} + \frac{\delta_{ij}}{3} \right). \tag{5}$$

By means of perturbations, the whole RST realizability space is explored, thus allowing for the estimation of turbulence closure uncertainty.

The perturbation of the eigenspace has tremendous physical implications that can lead to the development of radically different flows. In Mishra and Iaccarino (2019), authors established the physics based foundations of each individual perturbation, proving how perturbations sequentially change the original turbulence model. In this perspective, each perturbation generates a novel turbulence closure i.e., each perturbed solution should be considered as representative of a different turbulence model.

The EPM devised in Emory et al. (2011, 2013) entails finite perturbations of the eigenvalues of the BS closure. Namely, it varies the distribution of the spectral energy among eigenmodes. In this perspective, the realizability conditions establish a limit on the magnitude of eigenvalues perturbations. According to Banerjee et al. (2007), a convenient approach to enforce the realizability constraint consists in exploiting a barycentric reference frame. This particular choice allows for mapping the RST eigenvalues λ_i to a convex combination of the limiting states of turbulence componentiality $\mathbf{x}_{1C}$, $\mathbf{x}_{2C}$ and

$\mathbf{x}_{3C}$ through

$$\mathbf{x} = \mathbf{x}_{1C}\left(\lambda_1 - \lambda_2\right) + 2\mathbf{x}_{2C}\left(\lambda_2 - \lambda_3\right) + \mathbf{x}_{3C}\left(3\lambda_3 + 1\right). \tag{6}$$

In practice, $\mathbf{x}_{1C}$, $\mathbf{x}_{2C}$ and $\mathbf{x}_{3C}$ correspond to different limiting state of turbulence anisotropy. Namely, one-component flow (1C), where turbulent fluctuations exist along one direction only, axisymmetric two-components flow (2C), where fluctuations are present along two directions and with equal magnitude, and isotropic turbulence, corresponding to a three-components flow (3C). The work from Emory et al. (2011, 2013) was later extended by Iaccarino et al. (2017), to include a perturbation of the eigenvector orientation. No admissibility constraint concerns the orientation of the RST principal axes. Lastly, the overall spectral energy can be perturbed under the constraint of being a positive scalar quantity.

To keep the problem computationally tractable, we neglect variations of the overall spectral energy (retaining the value computed using the baseline closure), and we apply perturbations that do not explicitly depend on the spatial coordinate. In our settings, the EPM construction resembles the one reported in Mishra et al. (2018) and proceeds as follows. First, we force the repartition of energy between eigenmodes in order to attain one of the limiting states $\mathbf{x}_{1C}$, $\mathbf{x}_{2C}$, or $\mathbf{x}_{3C}$. Secondly, the principal axes of the perturbed RST are rotated so that the Frobenius inner product $\mathcal{F}$ between the anisotropic part of the RST model and the mean strain-rate tensor is alternatively minimized and maximized. According to Iaccarino et al. (2017), maximizing (resp. minimizing) this Frobenius inner product corresponds to maximizing (resp. minimizing) the production of turbulent kinetic energy. In the adopted framework, the EPM approach reduces to five possible pertur-

bations: $\mathcal{F}_{1C}^{max}$, $\mathcal{F}_{1C}^{min}$, $\mathcal{F}_{2C}^{max}$, $\mathcal{F}_{2C}^{min}$ and $3C$. Note that the extremal state $\mathbf{x}_{3C}$ corresponds to the isotropic component of the turbulence tensor; therefore its is invariant by rotation. Thereafter, we will adopt the following labels associated to five (perturbed) CFD simulations PA ($\mathcal{F}_{1C}^{max}$), PB ($\mathcal{F}_{2C}^{max}$), PC ($3C$), PD ($\mathcal{F}_{1C}^{min}$) and PE ($\mathcal{F}_{2C}^{min}$).

Once these five EPM simulations are carried out, a trustworthiness indicator, associated with a generic QoI p, can be defined as

$$\Delta_p \doteq \max(p^{\mathrm{PA}}, p^{\mathrm{PB}}, p^{\mathrm{PC}}, p^{\mathrm{PD}}, p^{\mathrm{PE}}) - \min(p^{\mathrm{PA}}, p^{\mathrm{PB}}, p^{\mathrm{PC}}, p^{\mathrm{PD}}, p^{\mathrm{PE}}). \qquad (7)$$

3. The NACA 0012 Test Case

The NACA 0012 airfoil is a classical reference test case for aerospace applications. The evaluation of its aerodynamic performances at the different Angle of Attack (AoA) allows assessing the domain of credibility of RANS predictions. Indeed, for large AoA, there is a transition in the flow regime, with the appearance of separated regions and large unsteady vortex structures that challenge turbulence closures. Moreover, given the prominent role of the NACA0012 in aeronautics, a large amount of qualitative and quantitative data are readily available. In particular, the NASA TMR (Turbulence Modeling Resource, http://turbmodels.larc.nasa.gov) offers a wide variety of resources that can be freely accessed and exploited, including numerical grids and experimental data. In particular, the test case of interest here corresponds to the 2DN00: 2D NACA 0012 Airfoil Validation Case in the NASA TMR database. We now recall the most prominent features of this test case and the numerical settings employed in simulations.

Table 1: Characteristics of the computational grids.

Label	N. points	N. elements	Type	TMR code
S_1	57824	57344	Structured	naca0012_0449x129
S_2	230336	229376	Structured	naca0012_0897x257
S_3	919424	917504	Structured	naca0012_1793x513
U_1	48664	57004	Hybrid	-
U_2	168345	188894	Hybrid	-
U_3	357641	397876	Hybrid	-

3.1. The Computational Model

The Reynolds number based on the free-stream Mach number $M_\infty = 0.15$, the static temperature $T_\infty = 300$ [K] and the reference chord length $c = 1$ [m], is $Re = 6 \cdot 10^6$. The Sutherland law models the variation of air viscosity w.r.t. temperature. The thermal conductivity is defined locally to ensure a constant Prandtl number. An adiabatic no-slip boundary condition is imposed at the airfoil boundary, whereas a turbulent to laminar viscosity ratio of 10.0 with 5% intensity of turbulent fluctuation applies at the far-field.

Because this work investigates the sensitivity of EPM uncertainty estimates to the finite spatial resolution, we consider a set of diverse structured and unstructured meshes. Table 1 summarizes the characteristics of the spatial meshes employed for the analysis.

In particular, we take advantage of the structured C-grids provided by the NASA TMR. Namely, the naca0012_449x129, the naca0012_897x257, and the naca0012_1793x513 meshes. The far-field boundary is approximately 500 chord lengths ahead and behind the airfoil. The grid resolution is sufficient

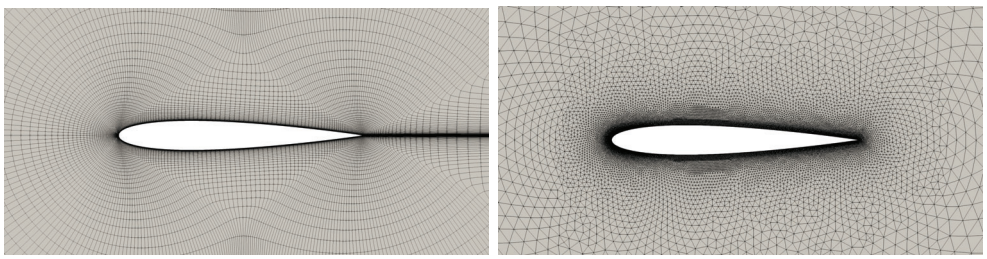

(a) (b)

Figure 1: Partial view of the numerical grid around the airfoil. (a) Mesh S_1. (b) Mesh U_1.

to resolve the boundary layer and capture the steep gradients with a first cell at the wall having a height of order 1 y^+. Figure 1(a) shows a partial view of the numerical grid around the airfoil. The unstructured hybrid grid generator employs an advancing-front/Delaunay algorithm implemented in an in-house meshing tool (Dussin et al., 2009). Quadrilateral elements are added in the neighborhood of the airfoil, to capture the viscous boundary layer. The cell size and growth laws near the wall resemble those of the NASA TMR FAMILY I. Figure 1(b) shows a partial view of the hybrid mesh around the airfoil.

3.2. Steady Solver

The open-source SU2 CFD solver (Palacios et al., 2013; Economon et al., 2016) was selected as it implements validated EPM capabilities (Mishra et al., 2018). The computation of the steady-state solution of the flow around the airfoil uses an implicit time-marching scheme. Numerical fluxes are computed by a generalized Approximate Riemann solver of Roe type, with a Monotone Upstream-centered Scheme for Conservation Laws (MUSCL) (Van Leer, 1979). The Venkatakrishnan flux limiter is employed to prevent and suppress

spurious oscillations. A two-level multi-grid approach is adopted to accelerate the numerical convergence of the iterations. The convergence to the steady-state solution is considered satisfactory when the variations of integrated normalized quantities, such as the lift and drag coefficients, remain below 10^{-3} over 100 iterations .

Figures 2(a) and 2(b) report, respectively, the lift C_L and drag C_D coefficients polar computed using mesh S_3. The continuous black lines correspond to the polars computed using the BS closure: the Menter's Shear Stress Transport (SST) model (Menter, 1993). The choice of the k-ω SST closure was forced as currently that is the only one with EPM capabilities in SU2. Nevertheless, it is worth to point out that the EPM approach is, in principle, agnostic to the turbulence closure, and that the above limitation is related only to current specific software implementation limits. In Figures 2(a) and 2(b), the gray shaded area depicts the estimated model trustworthiness indicator Δ_{C_L} and Δ_{C_D}. Colored lines indicate experimental measurements collected in different campaigns and made available in the NASA TMR. Namely, label AD stands for the Abbott and Doenhoff (1949) data (note that the AD data set proposes only lift measurements). Labels L1, L2, and L3 stand for Ladson's fixed transition experiments (Ladson, 1988). In these experiments, the transition was triggered by putting carborundum strips on the airfoil at 0.05 chord length. The indexes of Larson's experiments refer to a different size of grits in the carborundum strips (80, 120, and 180 for the L1, L2, and L3 experiments).

The plots of Fig. 2 show that RANS predictions are credible for small-to-medium AoAs. Indeed, for AoA smaller than 14 degrees, the uncertainty

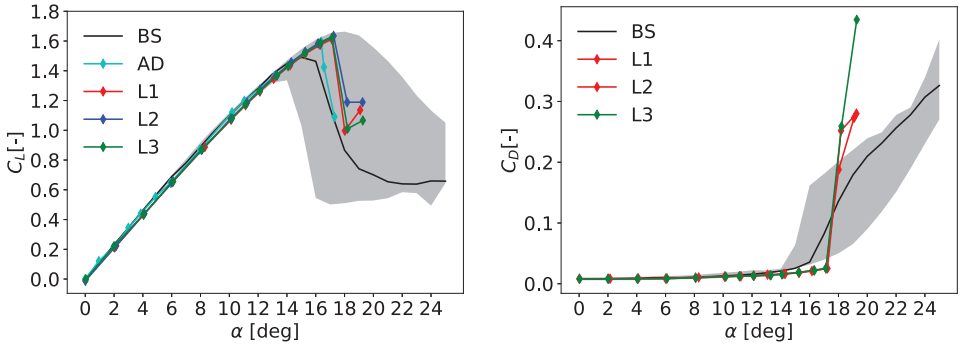

(a) (b)

Figure 2: Aerodynamic performance predictions (w.r.t the AoA), computed using the baseline closure (BS) , complemented by the envelope corresponding to the trustworthiness indicator Eq. (7) (gray shaded area). Experimental data are reported for comparison. (a) Lift coefficient C_L. (b) Drag Coefficient C_D.

envelope is somewhat limited, if not infinitesimal, and predictions match data well. In contrast, numerical predictions become unreliable for AoAs larger than 14 degrees. Though the baseline model still predicts lift and drag values close to the observations, the EPM envelope increases significantly past 14 degrees. This result is expected from knowing the physics of a high Reynolds flow around a slender body. For small AoAs, when gentle streamline curvature characterizes the flow field, the RANS model is accurate and reliable. On the contrary, at large AoAs the actual flow exhibits a strong curvature. At the limit, the flow can separate and become unsteady, causing the RANS model to lose credibility.

To provide physical insights, we report the EPM Turbulent Kinetic Energy (TKE) fields for the NACA 0012 airfoil at an AoA of 17 degrees, i.e., in the close proximity of the baseline stall angle. Picture 3(a-f) report, re-

spectively, the TKE field for the BS and the five EPM predictions (PA-PE). All pictures are focused on the airfoil leading edge. With reference to Fig. 3, perturbations corresponding to a maximized TKE production and concentrating the spectral energy in one (PA) or two (PB) modes only, respectively Fig. 3(a) and (b), foster the development of an attached flow similar to one resulting from the baseline solution. Indeed, the fields reported in Fig. 3(a-b-c) are qualitatively similar. Nevertheless, quantitative differences reveal that, in the perturbed models, the boundary layer is endowed with a higher kinetic energy content. Practically speaking, the maximization of TKE production increases the fluid apparent viscosity, fostering an early laminar-to-turbulent boundary layer transition which helps delaying stall. The isotropic turbulence model corresponding to perturbation PC predicts instead a stalled condition, Fig. 3(d). That is, an even distribution of the spectral energy among the RST modes causes an early flow separation, with detrimental consequences on the lift generated by the airfoil. Similarly, predictions associated to perturbations minimizing the production of TKE also reveal separated regions, see Fig. 3(e-f) reporting the solutions from the PD and PE models. Namely, suppressing TKE production results into a more or less accentuated separation of the flow over the airfoil.

3.3. Unsteady Solver

As seen from the analysis reported above, the airfoil reaches stall conditions for a high AoA, meaning that the flow detaches from the profile suction wall. In these conditions, the flow is unstable with large scale vortex shedding in the wake of the airfoil. In these conditions, the flow must be simulated with an Unsteady RANS (URANS) model. The URANS simulations

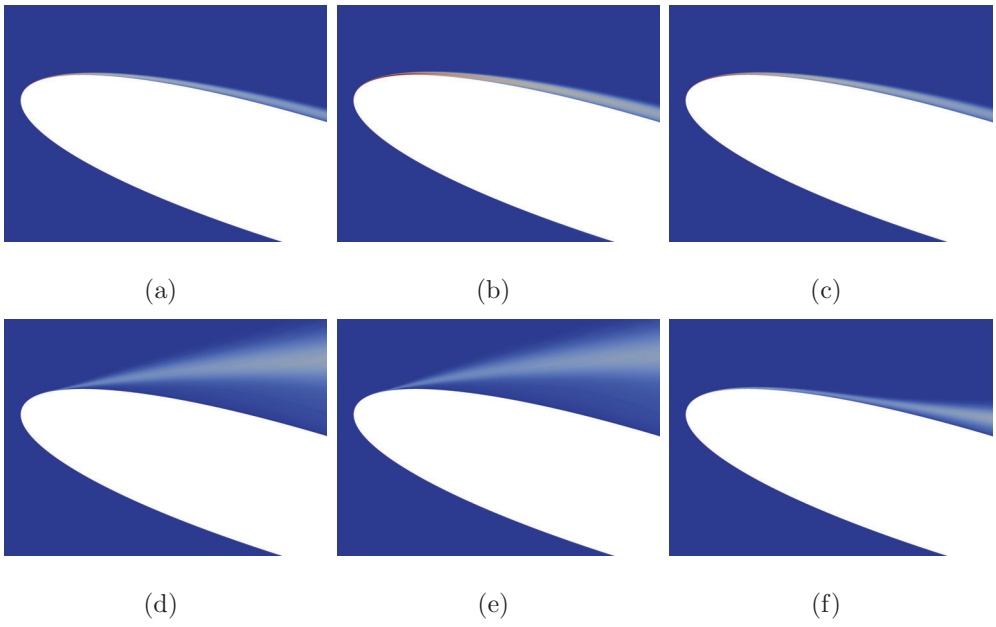

Figure 3: Aerodynamic TKE fields predicted by the EPM for the NACA0012 airfoil at an AoA of 17 degrees. (a) BS. (b) PA. (c) PB. (d) PC. (e) PD. (f) PE.

rely on a clear separation of time-scales: the time-scale of large turbulent structures (the vortex shedding from the airfoil) must be significantly longer than the fast random fluctuations modeled by the Reynolds-averaged quantities. Large turbulent structures are then resolved, whereas the RST model accounts for the impact of short-scale fluctuations.

In the reference test case considered here, we define the advection delay time-scale (τ_A). τ_A is related to the free stream velocity ($U_\infty \approx 52$ [m/s]) and characterizes the time for a fluid particle to travel one chord length c,

$$\tau_A = \frac{c}{U_\infty} \approx 0.02 \quad [\text{s}]. \tag{8}$$

The URANS simulations are employed to predict the unsteady flow field developing around the NACA 0012 airfoil at a high AoA. The unsteady com-

putational model is employed to simulate a time interval of $100 \cdot \tau_A = 2.0$ [s]. This long period is required to exhaust the initial transient state and obtain predictions independent of the arbitrary initial conditions. In unsteady simulations, the standard dual-time-stepping scheme, with second-order accuracy, from the SU2 CFD suite is employed to advance the solution in time. Figures 4(a-c) report the BS TKE field predictions for the NACA0012 airfoil at an AoA equal to 22 [deg], at three different time-steps within an interval $\Delta t = \tau_A$. URANS predictions expose the unsteady shedding of periodic large vortex structures downstream the airfoil.

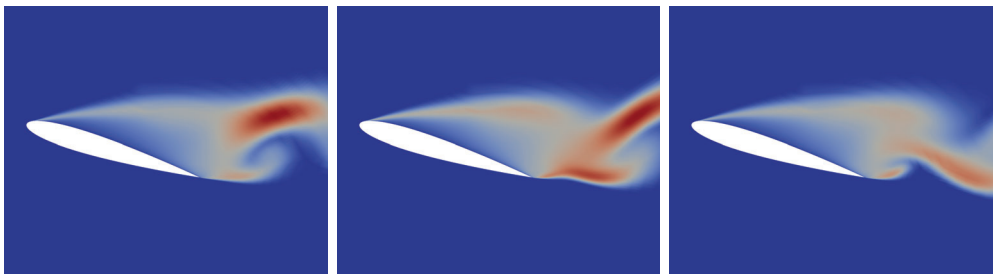

(a) (b) (c)

Figure 4: The unsteady aerodynamic TKE field predicted by the BS model for the NACA0012 airfoil at an AoA of 22 degrees. (a) $t = t_0 + 0.500$ [s]. (b) $t = t_0 + 0.510$ [s]. (c) $t = t_0 + 0.520$ [s].

4. Results

We first investigate in Section 4.1 the sensitivity of the EPM uncertainty estimates on the spatial discretization only, using the steady solver and considering a broad range of AoA, including stall conditions. Then, in Section 4.2, we select a stalled configuration and focus on the sensitivity of

the EPM uncertainty estimates on the simulation time-step, employing the URANS solver to simulate the unsteady flow fields.

4.1. Mesh Sensitivity Analysis

The sensitivity of the baseline solution is first assessed w.r.t. a different grid resolution, see Tab. 1. Figure 5(a) and (b) report a comparison of the lift and drag coefficients (C_L and C_D), respectively, predicted for different AoA, using different meshes. Predictions from all grids agree at low-to-medium AoA. Differences become significant for approximately $\alpha > 14$ degrees.

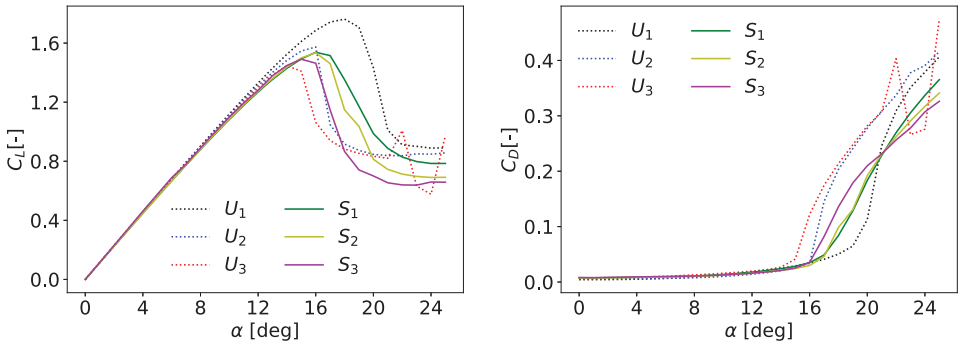

(a) (b)

Figure 5: Aerodynamic performance predictions (w.r.t the AoA) using the baseline turbulence closure, for different numerical grids. (a) Lift coefficient C_L. (b) Drag Coefficient C_D.

These discrepancies are due to the difficulties inherent the capturing of the stall. Namely, the BS predicted stall angle ranges from 14 to 19 degrees.

The same sensitivity study is carried out considering the five EPM simulations. Figure 6 reports the five polar graphs for lift (left column) and for drag (right column). Notably, the analysis reveals that EPM computations

are subject to a different sensitivity to the grid spatial resolution. Indeed, the C_L curves predicted by perturbed models envisaging the minimization of TKE production (PD and PE), and similarly by the one retaining an isotropic state of turbulence componentiality (PC), begin to suffer a significant dependency on the grid resolution at an AoA higher than about 12 [deg]. Instead, the same analysis carried out on the BS closure established the grid sensitivity threshold at about 14 [deg]. On the contrary, perturbations maximizing TKE production (PA and PB) appear to be less sensitive to the spatial resolution, showing mesh-independency up to an AoA of 16 degrees.

These empirical observations find physics based foundation in the work of Mishra and Iaccarino (2019), in which the authors show that eigenvalue and eigenvector perturbations extend an isotropic eddy viscosity model (such as the one employed in this work) to an orthotropic and anisotropic tensorial eddy viscosity model, respectively. In particular, perturbations towards the 1C and 2C extremal states produce an isotropic-to-orthotropic transformation of the eddy viscosity formulation while perturbations towards the 3C state retain the isotropic nature of the baseline turbulence closure. At the same time, the authors show that eigenvector perturbations possibly lead to obtaining a fully anisotropic eddy viscosity model. In brief, applying a particular perturbation is analogous to employing a different turbulence closure. For this reason, it should not be surprising that independent mesh sensitivity studies are required for each of the perturbed simulations.

Figure 7 reports a grid sensitivity analysis targeting the performance trustworthiness indicators of the lift (top) and drag coefficients (bottom).

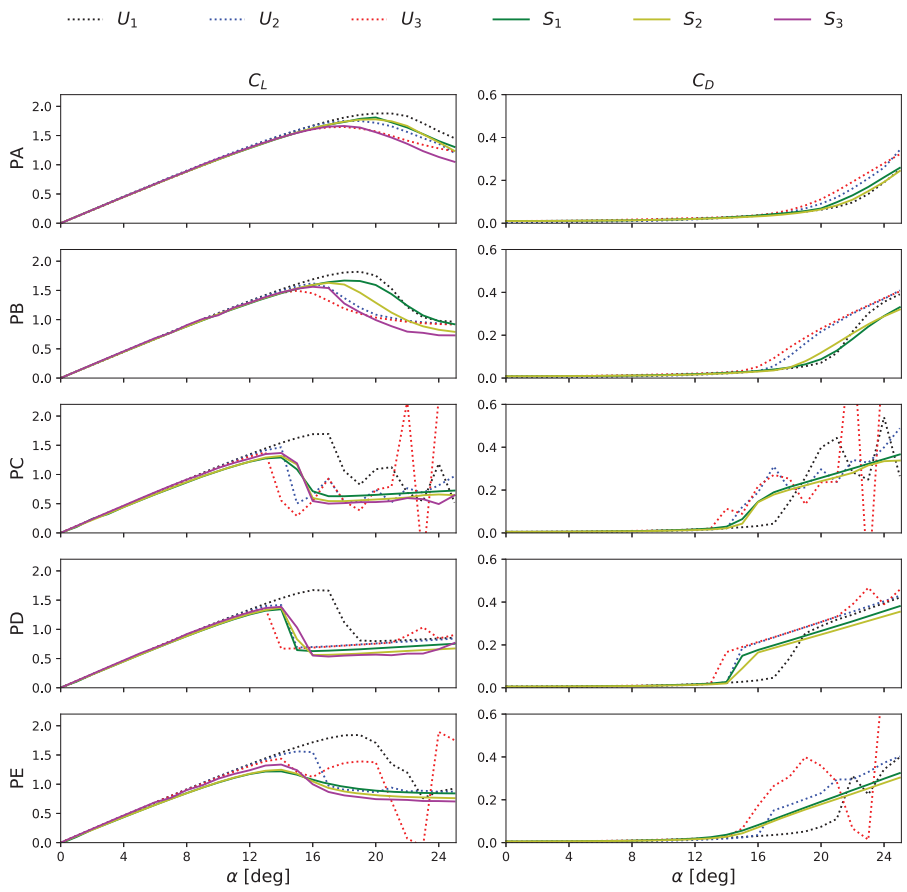

Figure 6: Aerodynamic performance predictions (w.r.t the AoA) using the EPM, for different numerical grids. (a) Lift coefficient C_L. (b) Drag coefficient C_D.

The plots confirm that the credibility indicators are independent from the mesh resolution for low-to-medium AoAs. On the contrary, at large AoA predictions seems to be characterized by a higher noise level. This is particularly true for predictions obtained by means of unstructured hybrid meshes, which are possibly liable for generating a higher numerical diffusivity. In general, results indicates that, for this test case, simulations taking advantage

of structured meshes are prone to provide more consistent predictions.

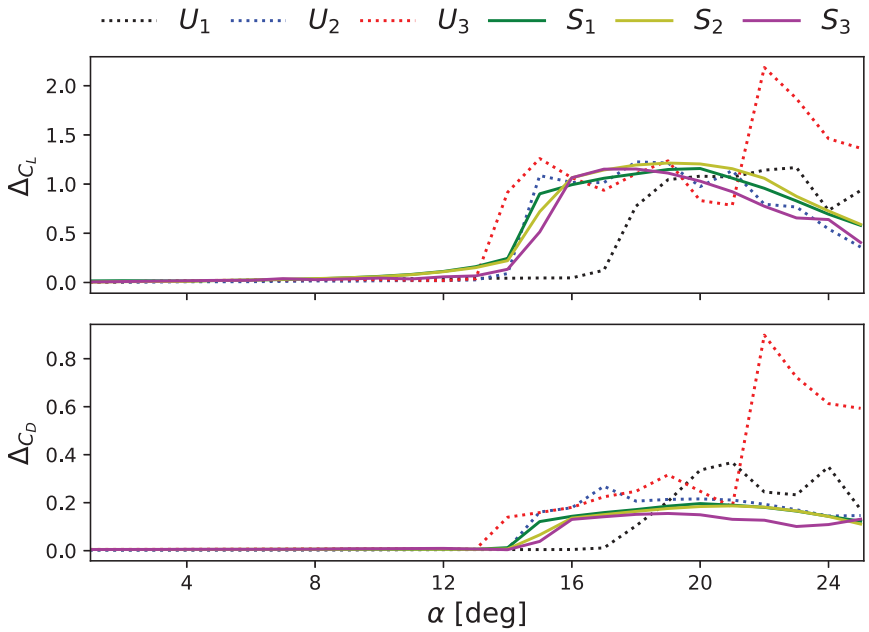

Figure 7: Percentage difference on aerodynamic performance trustworthiness indicator using different grids. The deviation is computed considering Δ_p predictions from grid S_3 as the reference. (Top) Deviation on ΔC_L, top. (Bottom) Deviation on ΔC_D.

4.2. Time-step Sensitivity Analysis

The sensitivity of numerical predictions of an unsteady turbulent flow are now assessed against the discretization time-step. All the results shown hereinafter are obtained using grid S_1 only. This choice is applied to lower the computational burden of unsteady simulations. As described in Sec. 3, the flow surrounding the NACA airfoil at a high AoA may be unsteady, with the shedding of large scale vortexes downstream the flow. Here, we

consider the NACA 0012 airfoil at an AoA of 22 degrees. Three different time-steps of increasing resolution are considered namely, $\Delta t = 1 \cdot 10^{-4}$ [s], $\Delta t = 2 \cdot 10^{-4}$ [s] and $\Delta t = 5 \cdot 10^{-4}$ [s]. First, the baseline solution is obtained, see Fig. 8(a). After an initial transitory phase, not shown in the plot and required to evolve the field from the initial steady guess to the unsteady regime, predictions of the targeted QoI (the lift coefficient C_L) sets on a periodic trend. The same oscillating behavior, with a small phase lag, is observed despite the time-step employed. The C_L value averaged over the whole simulation period corresponds to 1.065 for $\Delta t = 5 \cdot 10^{-4}$ [s], 1.054 for $\Delta t = 2 \cdot 10^{-4}$ [s] and 1.053 for $\Delta t = 1 \cdot 10^{-4}$ [s]. In Fig. 8(b), we report the Spectral Power Density (SPD) for the baseline signals. Note that, according to the Nyquist-Shannon sampling theorem, the employed time-steps allows to correctly capture frequencies up to, respectively, 5000, 2500 and 1000 [Hz]. Clearly, three frequency peaks are identifiable in the SPD plot, at about 28.9, 57.6 and 86.2 [Hz]. The plot shows also a good agreement among predictions obtained using different time-steps, for the fundamental harmonic. The estimation of higher frequency peaks requires instead a time-step of $\Delta t = 2 \cdot 10^{-4}$ at largest.

We now assess the EPM unsteady predictions w.r.t. the time-step. Figure 9 reports the five C_L signals (left column) complemented by the spectral power density plot (right column), for the three selected time-steps. Again, no significant differences are found in between solutions computed using time-steps of different size, except for a phase lag due to a different transient response w.r.t. the initial state.

Interestingly, simulations associated to a maximal TKE production (PA

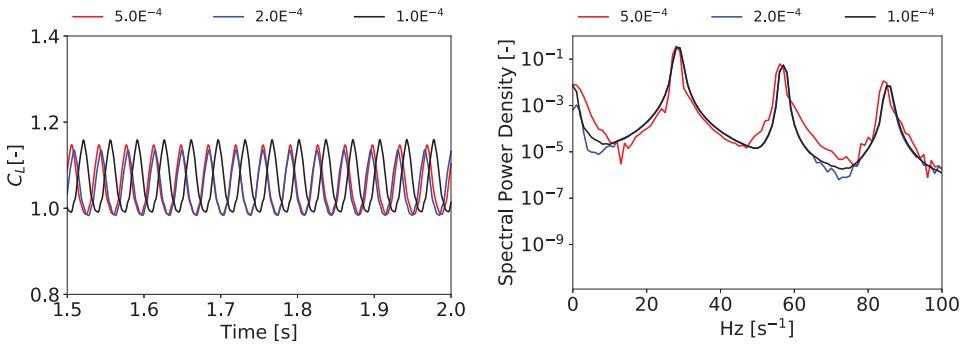

(a) (b)

Figure 8: Unsteady lift coefficient baseline predictions, for a NACA 0012 airfoil at AoA of 22 [deg]. (a) Lift coefficient signal over the 1.5-2.0 [s] period. (b) Spectral Power Density of the lift coefficient signal.

and PB) are associated to a steady signal, with a C_L corresponding respectively to about 1.78 and 1.26 (see Tab. 2 for the values specific to a different time-step), revealing that the effect of the eigenspace perturbation is to suppress the large scale unsteady fluctuations. On the contrary, the isotropic model (PC) and the models minimizing the TKE production (PD and PE) return a clearly periodic signal, with an average C_L of approximately 1.04, 1.02 and 1.15. Remarkably, we record a difference of about 0.75 between the maximum and the minimum average C_L predicted by the 5 EPM simulations. This behavior is coherent with the fact that the PA/PB perturbations maximize the production of turbulent kinetic energy and concentrate it into one or two modes only. Ultimately, this increases the fluid apparent viscosity, which helps delaying stall thus suppressing unsteady oscillations. On the other hand, perturbations that minimize the production of turbulent kinetic energy (PD/PE), and the one that spreads the energy equally among the

Table 2: Time-averaged C_L [-] values for the baseline and EPM unsteady simulations.

Δt [s]	BS	PA	PB	PC	PD	PE
$5 \cdot 10^{-4}$	1.0531	1.7813	1.2751	1.0320	1.0216	1.1418
$2 \cdot 10^{-4}$	1.0544	1.7794	1.2617	1.0341	1.0259	1.1413
$1 \cdot 10^{-4}$	1.0649	1.7780	1.2616	1.0363	1.0249	1.1453

three modes (PC), predict a separated flow field characterized by unsteady features. Table 2 gathers the C_L time-averaged values predicted using the baseline model and the five EPM perturbations.

By observing the spectral power density plot in Fig. 9, it is possible to point out differences in terms of energy distribution among harmonics. Beside the steady PA and PB cases, the spectral analysis reveals that frequency peaks vary depending on the applied perturbation. Compared to the baseline spectrum, PC and PD show a relatively more complicated dynamics, with the appearance of several additional frequency peaks. Peaks are found, for the shortest time-step, at 12.0, 24.7, 36.9, 49.4, 62.9, 75.6, 87.7 and 99.5 [Hz]. The SPD of PE is instead similar to the baseline one, showing three main harmonics only, with peaks located at 30.9, 62.2 and 92.7 [Hz].

Since the unsteady flow behavior is mainly governed by viscous turbulent effects, differences in EPM predictions were somehow expected given than the approach consists in perturbing the RST. The extent of such difference was instead surprising, especially because perturbations maximizing the production of TKE inhibit the unsteady features whereas the others appear to enrich the baseline signal with additional harmonics. Clearly, these findings call for an independent time-step sensitivity assessment of the five

EPM simulations. Indeed, there possibly might be a situation when the BS solution is steady, whereas some of the perturbed simulations are endowed with an unsteady behavior. In such cases, an assessment based on the sole analysis of the baseline solution would mislead to using the steady RANS solver. Instead, an analysis including the five EPM solutions would provide an indication that an unsteady RANS solver is required to correctly evaluate the role of the turbulence closure model-form uncertainty.

Eventually, we try to establish some measure to quantify the credibility of URANS predictions, showing how the turbulence model trustworthiness indicator varies w.r.t. the simulation time-step. Note that, currently, there is no clear strategy for quantifying the URANS model credibility w.r.t. the turbulence closure. Here, we adopt the arbitrary choice of analyzing the cross-correlation and coherence among the five EPM signals. Namely, in signal processing cross-correlation is typically employed to measure the similarity of two signals as a function of the displacement of one relative to the other. That is, cross-correlation can be exploited to find the delay between two signals or to search a long signal for a shorter. In this perspective, we employ cross-correlation to measure the similarity between the five EPM signals, for a given grid. Similarly, coherence is a statistic expressing the correlation between two signals as a function of the frequency components which they contain. In other words, it expresses the correlation of the signal w.r.t. the spectral energy distribution. In Fig. 10(a) we report a chart-bar indicating the maximum cross-correlation among all the possible signal combinations, for the different time-steps. As mentioned, cross-correlation can be interpreted as a measure of signal similarity as a function of a variable

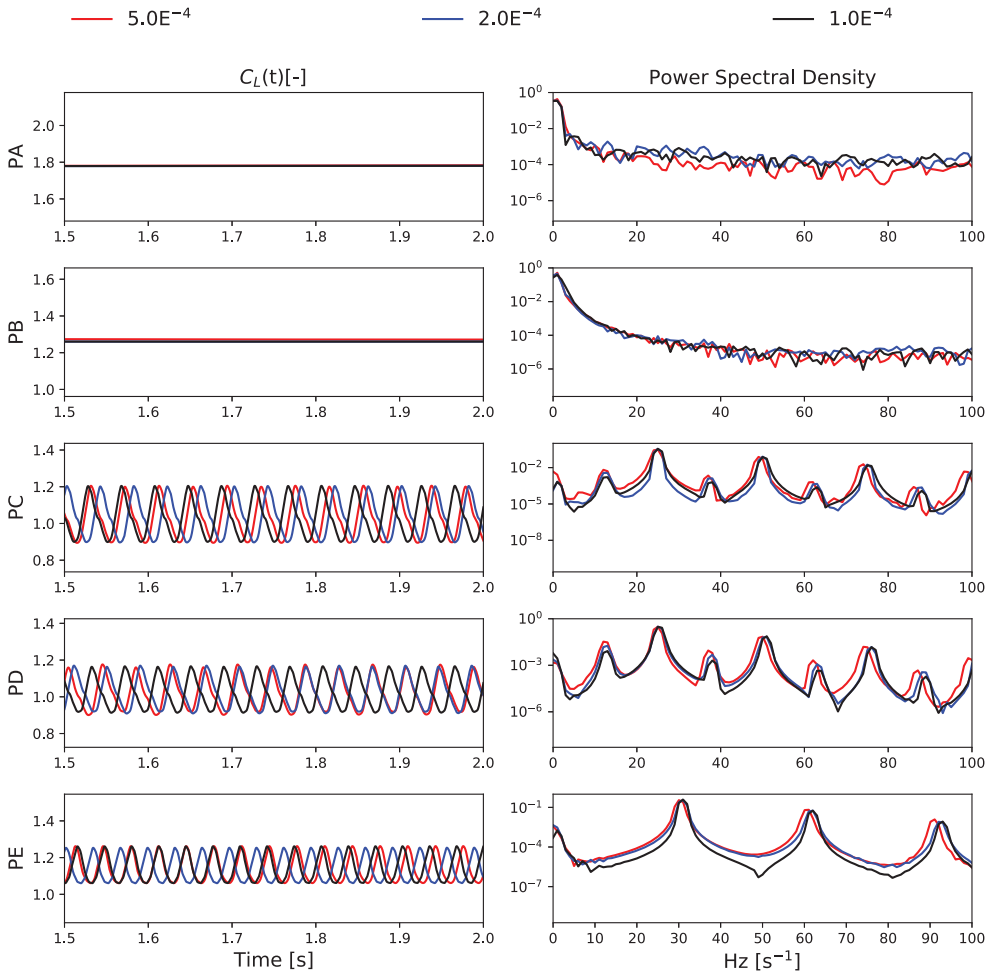

Figure 9: Unsteady lift coefficient EPM predictions, for a NACA 0012 airfoil at AoA of 22 [deg], for the three time-steps. (a) Lift coefficient signal over the 1.5-2.0 [s] period. (b) Spectral Power Density of the lift coefficient signal.

time lag. The maximum of the cross-correlation function indicates the delay that would allow for the best signal matching. Clearly, signals are generally uncorrelated with the exception of PA-PB and PC-PD. Surely, the maximum

cross-correlation is always lower than one, meaning that there is no finite time shift leading to a perfect alignment of two EPM signals. Nevertheless, by excluding the PA-PB combination, which represent the special case involving steady signals (and possibly highly sensitive to numerical noise) the bar chart reveals a quite robust convergence w.r.t. the time-step. Figure 10(b) reports instead the maximum signals coherence in between the 0-100 Hertz range. Coherence can be interpreted as a measure of the similarity of two signals in terms of spectral energy distribution. Note that coherence is a function of the frequency. Here, we report only its maximum. Not surprisingly, the PC, PD and PE signals show a higher coherence due to the fact that some of the peaks in the SPD diagrams are located in the proximity of the very same frequencies. Among PC-PE and PD-PE, coherence diminishes with the time resolution, possibly because so does leakage around frequency peaks in the PE signal. The slightly better separation of the harmonics in the PE signal lessen the coherence with PC and PD.

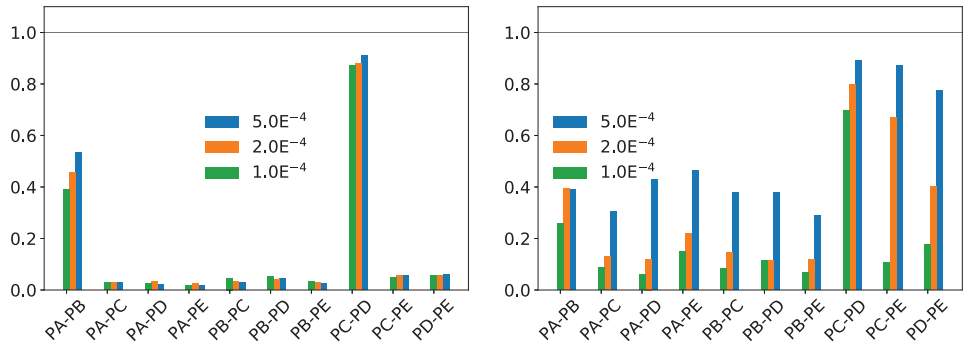

(a) (b)

Figure 10: EPM unsteady signals similarity assessment, for the NACA 0012 airfoil at AoA of 22 [deg]. (a) Signals cross-correlation. (b) Signals coherence.

5. Conclusions

This paper presents an investigation of the sensitivity of structural turbulence uncertainty estimates, obtained by means of the Eigenspace Perturbation Method, w.r.t. the time and space resolution of numerical computations. Result show that, in general, one can not expect the EPM and the baseline solutions to exhibit the same grid/time resolution dependency. The recommendation is to carry out independent sensitivity studies on each of the five EPM simulations, to guarantee that the confidence uncertainty estimates are well-predicted regardless of the space and time resolution. If reasonable, the use of a different numerical set up, tailored to each of the EPM perturbations, is advised. We stress here, once again, that the EPM only returns uncertainty estimates rather than provable and rigorous bounds. In this regards, one is never interested in a precise computation of the five EPM solutions themselves, but rather in retrieving an indication about their dispersion around the baseline prediction. The rationale underlying the necessity of conducting independent sensitivity studies should be ensuring that the magnitude of the uncertainty estimates i.e., the prediction dispersion, is actually due to the turbulence closure structure uncertainty, and not to numerical artifacts. Future work may be pledged in investigating different types of perturbation, including for instance those characterized by a spatial variability.

Acknowledgements

This research was funded by the UTOPIAE Marie Curie Innovative Training Network, H2020-MSCA-ITN-2016, Grant Agreement number 722734. Experiments presented in this paper were carried out using the PlaFRIM

experimental testbed, supported by Inria, CNRS (LABRI and IMB), Université de Bordeaux, Bordeaux INP and Conseil Régional d'Aquitaine (see https://www.plafrim.fr/)

References

K. Duraisamy, G. Iaccarino, H. Xiao, Turbulence modeling in the age of data, Annual Review of Fluid Mechanics 51 (2019). doi:10.1146/annurev-fluid-010518-040547.

H. Xiao, P. Cinnella, Quantification of model uncertainty in rans simulations: A review (2019).

A. J. Simonsen, P. A. Krogstad, Turbulent stress invariant analysis: Clarification of existing terminology, Physics of Fluids 17 (2005) 088103. doi:10.1063/1.2009008.

U. Schumann, Realizability of Reynolds stress turbulence models, The Physics of Fluids 20 (1977) 721–725. doi:10.1063/1.861942.

M. Emory, R. Pecnik, G. Iaccarino, Modeling structural uncertainties in reynolds-averaged computations of shock/boundary layer interactions, 2011. doi:10.2514/6.2011-479.

M. Emory, J. Larsson, G. Iaccarino, Modeling of structural uncertainties in reynolds-averaged navier-stokes closures, Physics of Fluids 25 (2013) 110822. doi:10.1063/1.4824659.

S. Banerjee, R. Krahl, F. Durst, C. Zenger, Presentation of anisotropy properties of turbulence, invariants versus eigenvalue approaches, Journal of Turbulence 8 (2007). doi:10.1080/14685240701506896.

G. Iaccarino, A. Mishra, S. Ghili, Eigenspace perturbations for uncertainty estimation of single-point turbulence closures, Physical Review Fluids 2 (2017). doi:10.1103/PhysRevFluids.2.024605.

A. A. Mishra, G. Iaccarino, Theoretical analysis of tensor perturbations for uncertainty quantification of reynolds averaged and subgrid scale closures, Physics of Fluids 31 (2019) 075101. URL: https://doi.org/10.1063/1.5099176. doi:10.1063/1.5099176. arXiv:https://doi.org/10.1063/1.5099176.

A. Mishra, J. Mukhopadhaya, G. Iaccarino, J. J. Alonso, An uncertainty estimation module for turbulence model predictions in SU2, AIAA Journal (2018). doi:10.2514/1.J057187.

D. Dussin, M. Fossati, A. Guardone, L. Vigevano, Hybrid grid generation for two-dimensional high-reynolds flows, Computers & Fluids 38 (2009) 1863–1875.

F. Palacios, J. J. Alonso, K. Duraisamy, M. Colonno, J. Hicken, A. Aranake, A. Campos, S. Copeland, T. D. Economon, A. Lonkar, T. Lukaczyk, T. Taylor, Stanford University Unstructured (SU^2): An open-source integrated computational environment for multi-physics simulation and design, AIAA Paper 2013-0287 (2013).

T. D. Economon, D. Mudigere, G. Bansal, A. Heinecke, F. Palacios, J. Park, M. Smelyanskiy, J. J. Alonso, P. Dubey, Performance optimizations for scalable implicit RANS calculations with SU2, Computers & Fluids 129 (2016) 146 – 158.

B. Van Leer, Towards the ultimate conservative difference scheme. v. a second-order sequel to godunov's method, Journal of computational Physics 32 (1979) 101–136.

F. Menter, Zonal two equation $k - \omega$, turbulence models for aerodynamic flows, AIAA Paper (1993).

I. H. A. Abbott, A. E. Doenhoff, Theory of wing section; including a summary of airfoil data, 1949.

C. Ladson, Effects of independent variation of Mach and Reynolds numbers on the low-speed aerodynamic characteristics of the NACA 0012 airfoil section, National Aeronautics and Space Administration, Langley Research Center, Hampton, VA (1988) L–16472, NAS 1.15: 4074.